The Effect of Dielectric Loss in FDTD Simulations of Microstrip Structures

David C. Wittwer, *Member, IEEE,* and Richard W. Ziolkowski, *Fellow, IEEE*

***Abstract*—The importance of dielectric losses in planar microstrip structures is evaluated with the finite-difference time-domain (FDTD) method. This analysis was previously not possible in many FDTD simulators due to a lack of absorbing boundary conditions (ABCs), which appropriately terminate air/dielectric interfaces for which the dielectric is lossy. The newly proposed lossy two-time derivative Lorentzian material (L2TDLM) model ABC allows for these terminations and is presented and implemented here for three-dimensional FDTD simulations. The effect of dielectric losses on several well-known planar microstrip structures is evaluated. It is shown that the inclusion of these losses in FDTD simulations, which is facilitated by the L2TDLM ABC, is, in fact, important to predict the performance of resonant structure on lossy dielectric substrates.**

***Index Terms*—Finite-difference methods, microwave circuits, microwave measurements, numerical analysis.**

I. Introduction

CONSIDERABLE effort has been expended in recent years both in the computational electromagnetics (CEM) [1]–[16] and applied mathematics communities [17]–[19] toward the construction of highly efficient absorbing boundary conditions (ABCs) for reflectionless grid truncation of numerical simulators for Maxwell's equations. Ideally, the perfect ABC would absorb electromagnetic energy incident from any angle, with any polarization and at all frequencies. Reflectionless termination of simulation regions associated with, for instance, the finite-difference time-domain (FDTD) method and finite-element method (FEM) require such ABCs. Generally the perfectly matched layer (PML) or the related uniaxial ABCs have only been applied to terminate lossless regions of the simulation space.

Unfortunately, many practical simulation problems involving, for instance, microstrip transmission lines, microstrip patch antennas, and microwave integrated circuits (MICs)/millimeter-wave integrated circuits (MMICs), deal with lossy substrates. Accurate simulations of these problems necessitate termination of the simulation region with an ABC matched to these lossy dielectrics. Several papers have appeared recently [1], [2], [20]–[25], which have established the need for such lossy-media ABCs and have proposed partial or complete solutions. We present a summary of the complete Maxwellian material-based three-dimensional (3-D) FDTD ABC for lossy media developed in [1] and [2], compare it to other approaches, in particular with Gedney's uniaxial perfect matched layer (UPML) ABC, and apply it to the simulation of the behavior of several microwave circuit elements printed on lossy substrates.

A summary of the generalized formulation for the lossy two-time derivative Lorentz material (L2TDLM) model and its coupling to Maxwell's equations is discussed in Section II. Like the previous developments in [1] and [2], we characterize a face (or slab) by its normal and introduce additional loss in that direction with an increasing profile function. To achieve a complete ABC, we introduce the requisite formulation for a corner (union of three faces, hence, depending on three independent loss profile parameters). This formulation reduces to the lossless case when the conductivity of the media becomes zero and which further reduces to Maxwell's equations in free space as the permittivity goes to unity and, hence, recovers the 3-D two-time derivative Lorentz material (TDLM) ABC developed in [16]. It is highly desirable from a numerical implementation point-of-view to arrive at a formulation that has these properties. Furthermore, it is also highly convenient from an implementation point-of-view to have a formulation for a corner that reduces uniquely to the correct edge (union of two faces, hence, depending on two independent loss profile parameters) formulation and which further reduces uniquely to the correct face formulation with the appropriate selection of parameters. This avoids having separate formulations for each region and, hence, makes the ABC very efficient to implement algorithmically and reduces the coding complexity. The numerical implementation of the L2TDLM ABC is summarized in Section III. Several validation problems dealing with sources and propagation in lossy media in opened and closed 3-D regions are discussed in [1]. Comparisons between the L2TDLM ABC and the UPML ABC results for the two-dimensional (2-D) lossy interface problem emphasized by Gedney in [20] and ([25, Ch. 5] are given in Section IV. It is shown that the L2TDLM and the UPML ABCs produce comparable results for this 2-D problem. In addition to providing absorption levels at least as favorable as other methods, the L2TDLM formulation also allows for the possibility of providing an approach to achieving potentially physically realizable materials for absorbers using the artificial material constructs discussed, for instance, in [26] and [27]. Moreover, as shown in [1], it also has the favorable characteristic that it minimizes or eliminates

Manuscript received October 6, 1998. The work of D. C. Wittwer was supported in part by the Radar Design Center, Raytheon Systems Company, under the Doctoral Fellowship Program. The work of R. W. Ziolkowski was supported in part by the Office of Naval Research under Grant N0014-95-1-0636 and by the Air Force Office of Scientific Research, Air Force Material Command, USAF, under Grant F49620-96-1-0039.

D. C. Wittwer is with the Assembly Test and Development Group, Intel Corporation, Chandler, AZ 85226-3699 USA (e-mail: david.c.wittwer@intel.com).

R. W. Ziolkowski is with the Electromagnetics Laboratory, Department of Electrical and Computer Engineering, University of Arizona, Tucson, AZ 85721-0104 USA (e-mail: ziolkowski@ece.arizona.edu).

Publisher Item Identifier S 0018-9480(01)01065-1.

the late time slow growth in the numerical errors associated with the UPML ABC noted in [25, Ch. 5]. The resulting FDTD simulator has been applied to several microwave structures, including a microstrip low-pass filter, microstrip branch-line coupler, microstrip line-fed rectangular patch antenna, and microstrip rectangular spiral inductor. A summary of these simulations is also given in Section IV. Comparisons between cases in which the substrates associated with each of these structures are lossless, slightly lossy, and very lossy are made. Validation of simulated results is obtained through comparison with measured results. A brief discussion of how the devices were fabricated and measured is included to allow for proper comparison with the simulated results. The importance of including the loss in the prediction of the performance of these microstrip structures is emphasized. A summary of our conclusions is presented in Section V.

II. Effective ABC for Lossy Dielectrics

Our foundation for engineering an absorbing material for use as an ABC is based on the coupling of the electric and magnetic fields to polarization and magnetization currents. The coupling coefficients of the polarization and magnetization currents that describe these interactions are then free parameters, which may be specified in such a way as to provide a reflectionless boundary between the surrounding homogeneous medium and absorbing layer, which, following [9], is taken to be an uniaxial medium. Furthermore, the loss in the absorbing medium can be enhanced by varying the independent parameters of the polarization and magnetization currents as functions (profiles) of position away from an interface along the normal direction to that interface [1], [2], [13]–[16].

A. Matched Lossy Uniaxial Material

We wish to match a lossy dielectric medium to a uniaxial medium. The frequency-domain Maxwell's equations describing this uniaxial medium can be expressed in the following form:

$$\nabla\times\vec{\mathcal{E}}=-j\omega\left[\,\overline{\overline{\mu}}\,\right]\vec{\mathcal{H}}-\sigma^{*}\vec{\mathcal{H}}$$
$$\nabla\times\vec{\mathcal{H}}=j\omega\left[\,\overline{\overline{\epsilon}}\,\right]\vec{\mathcal{E}}+\sigma\vec{\mathcal{E}}$$

where we have defined, as in [1] and [2], the tensors $\overline{\overline{\epsilon}}$ and $\overline{\overline{\mu}}$ for an interface with an x-, y-, z-directed normal, respectively, by

$$\frac{\overline{\overline{\epsilon}}}{\epsilon_0}=\widehat{\epsilon_r}\begin{pmatrix}1/a_x & & \\ & a_x & \\ & & a_x\end{pmatrix}=\widehat{\epsilon_r}\overline{\overline{\Lambda_x}}\qquad\frac{\overline{\overline{\mu}}}{\mu_0}=\widehat{\mu_r}\overline{\overline{\Lambda_x}}$$
$$\frac{\overline{\overline{\epsilon}}}{\epsilon_0}=\widehat{\epsilon_r}\begin{pmatrix}a_y & & \\ & 1/a_y & \\ & & a_y\end{pmatrix}=\widehat{\epsilon_r}\overline{\overline{\Lambda_y}}\qquad\frac{\overline{\overline{\mu}}}{\mu_0}=\widehat{\mu_r}\overline{\overline{\Lambda_y}}$$
$$\frac{\overline{\overline{\epsilon}}}{\epsilon_0}=\widehat{\epsilon_r}\begin{pmatrix}a_z & & \\ & a_z & \\ & & 1/a_z\end{pmatrix}=\widehat{\epsilon_r}\overline{\overline{\Lambda_z}}\qquad\frac{\overline{\overline{\mu}}}{\mu_0}=\widehat{\mu_r}\overline{\overline{\Lambda_z}}\qquad(1)$$

where all of the off-diagonal terms are zero, the terms $\widehat{\epsilon_r}=\epsilon_r-j\sigma/\omega\epsilon_0$ and $\widehat{\mu_r}=\mu_r-j\sigma^{*}/\omega\mu_0$. As was done in [1] and [2], these tensors are rewritten in terms of electric and magnetic susceptibility tensors

$$\overline{\overline{\chi^{e}}}=\frac{\overline{\overline{\epsilon}}}{\epsilon_0}-\overline{\overline{1}}\qquad\overline{\overline{\chi^{m}}}=\frac{\overline{\overline{\mu}}}{\mu_0}-\overline{\overline{1}}.\qquad(2)$$

We choose the absorber medium to be described by the two-time derivative Lorentz material model for lossy dispersive media [1], [2] denoted by L2TDLM, where time derivatives of the driving fields act as source terms to describe the coupling of the electric and magnetic fields to the polarization and magnetization fields [13]–[16]. These polarization- and magnetization-field models are represented in differential form as

$$\frac{\partial^2}{\partial t^2}\mathcal{P}_x+\Gamma\frac{\partial}{\partial t}\mathcal{P}_x+\omega_o^2\mathcal{P}_x=\epsilon_0\left(\omega_p^2\chi_\alpha^e\mathcal{E}_x+\omega_p\chi_\beta^e\frac{\partial}{\partial t}\mathcal{E}_x+\chi_\gamma^e\frac{\partial^2}{\partial t^2}\mathcal{E}_x\right)\qquad(3)$$

$$\frac{\partial^2}{\partial t^2}\mathcal{M}_x+\Gamma\frac{\partial}{\partial t}\mathcal{M}_x+\omega_o^2\mathcal{M}_x=\omega_p^2\chi_\alpha^m\mathcal{H}_x+\omega_p\chi_\beta^m\frac{\partial}{\partial t}\mathcal{H}_x+\chi_\gamma^m\frac{\partial^2}{\partial t^2}\mathcal{H}_x\qquad(4)$$

where ω_0 is the resonance frequency and $\Gamma^{e,m}$ is the width of that resonance. The terms $\chi_\alpha^{e,m}$, $\chi_\beta^{e,m}$, and $\chi_\gamma^{e,m}$ represent, respectively, the coupling of the electric (magnetic) field and its first- and second-time derivatives to the local polarization (magnetization) fields. The term ω_p can be viewed as the plasma frequency associated with this coupling. It has been shown in [13] that if $\omega\gg\omega_0$, then the frequency-domain electric and magnetic susceptibilities associated, for instance, with (3) and (4), may be approximated in the frequency domain by

$$\chi_{xx}^{e}(\omega)=\frac{\mathcal{P}_x}{\epsilon_0\mathcal{E}_x}\approx-\frac{\omega_p^2}{\omega^2}\chi_\alpha^e-j\frac{\omega_p\chi_\beta^e}{\omega}+\chi_\gamma^e$$
$$\chi_{xx}^{m}(\omega)=\frac{\mathcal{M}_x}{\mathcal{H}_x}\approx-\frac{\omega_p^2}{\omega^2}\chi_\alpha^m-j\frac{\omega_p\chi_\beta^m}{\omega}+\chi_\gamma^m.$$

Following the arguments in [1] and [2], this material is readily matched to a lossy dielectric characterized by the material constants $\epsilon=\epsilon_r\epsilon_0$, $\mu=\mu_0$ and σ. One finds that matching is achieved when the free parameters in the L2TDLM model are given by the expressions

$$\begin{aligned}\omega_p^2\chi_\alpha^m&=0\\ \omega_p^2\chi_\alpha^e&=(\sigma/\epsilon_0)\omega_p\chi_\beta^m=(\sigma/\epsilon_0)\rho_{\max}\rho(\vec{r})\\ \omega_p\chi_\beta^m&=\rho_{\max}\rho(\vec{r})\\ \omega_p\chi_\beta^e&=\sigma/\epsilon_0+\epsilon_r\omega_p\chi_\beta^m=(\sigma/\epsilon_0)+\epsilon_r\rho_{\max}\rho(\vec{r})\\ \chi_\gamma^m&=0\\ \chi_\gamma^e&=\epsilon_r-1.\end{aligned}\qquad(5)$$

The term $\omega_p\chi_\beta^m$ is taken as a single quantity and is composed of a profile $\rho(\vec{r})$ for increasing the loss while moving away from the interface along the normal direction and the profile maximum $\rho_{\max}$. For all the cases considered below, the profile was taken to be a quadratic function of the distance away from the interface. These parameters represent the only independent values that must be specified to define the absorbing ABC layer. We also note that the form of the electric susceptibility now reduces to the lossless case in the absence of the conductivity term. Furthermore, the electric susceptibility now

reduces to the free-space result as the permittivity approaches unity.

B. L2TDLM ABC Equation Set

Following the work presented in [1], we derive an ABC suitable for use with lossy dielectrics by systematizing the above matching conditions to face, edge, and corner regions. As noted above, we characterize a face (or slab) by its normal and introduce additional loss in that direction with the increasing profile function $\rho(\vec{r})$. To achieve a complete ABC, we must also introduce the requisite formulation for the edges (union of two faces, hence, depending on two independent loss profile parameters) and for the corners (union of three faces, hence, depending on three independent loss profile parameters). We have achieved a formulation that reduces to the lossless case when the conductivity of the media becomes zero and which further reduces to Maxwell's equations in free space as the permittivity goes to unity and, hence, recovers the 3-D TDLM ABC developed in [16]. It is highly desirable from a numerical implementation point-of-view to arrive at a formulation that has these properties. Furthermore, it is also highly convenient from an implementation point-of-view to have a formulation for a corner that reduces uniquely to the correct edge formulation and which further reduces uniquely to the correct face formulation with the appropriate selection of parameters. This avoids having separate formulations for each region, hence, makes the ABC very efficient to implement algorithmically and reduces the coding complexity. Finally, the formulation developed for the corner region reduces to the edge and face formulations as the appropriate parameters go to zero.

Let the profiles along the $+\hat{x}$-, $+\hat{y}$-, and $+\hat{z}$-directions be denoted, respectively, by $\xi(x) = \rho_{\max,x}(x - x_{\rm start})^2/(x_{\rm end} - x_{\rm start})^2$, $\eta(y) = \rho_{\max,y}(y - y_{\rm start})^2/(y_{\rm end} - y_{\rm start})^2$, and $\zeta(z) = \rho_{\max,z}(z - z_{\rm start})^2/(z_{\rm end} - z_{\rm start})^2$. For all the cases treated below, we have set $\rho_{\max,x} = \rho_{\max,y} = \rho_{\max,z} = \rho_{\max}$. Now, consider the union of three slabs of absorber, each with a face normal to the $+\hat{x}$-, $+\hat{y}$-, and $+\hat{z}$-directions. To prevent reflections from a corner, the electric and magnetic susceptibilities must have the forms

$$\overline{\overline{\chi^e}} = \hat{\epsilon_r}\overline{\overline{\Lambda_x}} \times \overline{\overline{\Lambda_y}} \times \overline{\overline{\Lambda_z}} - \overline{\overline{1}}$$
$$\overline{\overline{\chi^m}} = \overline{\overline{\Lambda_x}} \times \overline{\overline{\Lambda_x}} \times \overline{\overline{\Lambda_z}} - \overline{\overline{1}}.$$

The magnetization terms are identical to those treated in [16]. The polarization terms must be handled as shown in [1]. From the above definition of the permittivity, it is seen one only need consider one field component as the other two may be obtained by cyclic permutations of the variables. After a number of manipulations discussed in [1], the equations for the z-component of the electric field in the corner region becomes

$$\partial_t \mathcal{E}_z + \left[\frac{\sigma}{\epsilon_r\epsilon_o} + (\xi+\eta)\right]\mathcal{E}_z = \frac{1}{\epsilon_r\epsilon_o}\left(\nabla\times\vec{\mathcal{H}}\right)_z - \frac{1}{\epsilon_r\epsilon_o}\mathcal{J}_z \tag{6}$$

$$\partial_t \mathcal{J}_z = -\zeta\left(\nabla\times\vec{\mathcal{H}}\right)_z + \left[\epsilon_r\epsilon_o\xi\eta + \sigma(\xi+\eta)\right]\mathcal{E}_z + \mathcal{F}_z \tag{7}$$

$$\partial_t \mathcal{F}_z = \sigma\xi\eta\mathcal{E}_z. \tag{8}$$

The current $\mathcal{J}_z$ is introduced to provide the fields that cancel the original field. The function $\mathcal{F}_z$ is an auxiliary function, which is introduced because of the order of the ordinary differential equation that was derived for the polarization field $\mathcal{P}_z$. We note that these equations do not explicitly involve that polarization field, but rather only the corresponding polarization current terms $\mathcal{J}_z$ and $\mathcal{F}_z$. Similar equations for the x- and y-components are obtainable from this set by a cyclic permutation of the variables and associated parameters.

We also note that, if in the corner equations we set $\eta = 0$ (or $\xi = 0$ or $\zeta = 0$), which would be appropriate for the corner reducing to an $x - z$ edge (or $y - z$ edge or $x - y$ edge, respectively), the equations for that edge are recovered. Similarly, the corner equations with two profile parameters set to zero or the edge equations with one profile parameter set to zero recover the corresponding face equations. This self-consistency of the equations significantly reduces the complexity of coding the L2TDLM ABC.

III. FDTD Implementation

These polarization, magnetization, and auxiliary field rate equations are implemented into a FDTD simulator by obtaining their discrete forms using finite differences. Consider, for instance, the above z-component set of equations for the corner. If we let these fields be located at $\mathcal{E}_z^{n,n+1}$, $\mathcal{J}_z^{n,n+1}$, and $\mathcal{F}_z^{n+1/2}$, and introduce an exponential difference scheme, this system can be manipulated into forms that yield the following semi-implicit update equations:

$$\mathcal{E}_z^{n+1} = \frac{a_{22}b_{11} - a_{12}b_{21}}{\det\left(\overline{\overline{A}}\right)}\mathcal{E}_z^n + \frac{a_{22}c_{11} - a_{12}c_{21}}{\det\left(\overline{\overline{A}}\right)} \cdot \left(\nabla\times\vec{\mathcal{H}}\right)_z^{n+1/2} + \frac{a_{22}b_{12} - a_{12}b_{22}}{\det\left(\overline{\overline{A}}\right)}\mathcal{J}_z^n + \frac{a_{22}c_{12} - a_{12}c_{22}}{\det\left(\overline{\overline{A}}\right)}\mathcal{F}_z^{n+1/2} \tag{9}$$

$$\mathcal{J}_z^{n+1} = \frac{a_{11}b_{22} - a_{21}b_{12}}{\det\left(\overline{\overline{A}}\right)}\mathcal{J}_z^n + \frac{a_{11}c_{21} - a_{21}c_{11}}{\det\left(\overline{\overline{A}}\right)} \cdot \left(\nabla\times\vec{\mathcal{H}}\right)_z^{n+1/2} + \frac{a_{11}b_{21} - a_{21}b_{11}}{\det\left(\overline{\overline{A}}\right)}\mathcal{E}_z^n + \frac{a_{11}c_{22} - a_{21}c_{12}}{\det\left(\overline{\overline{A}}\right)}\mathcal{F}_z^{n+1/2} \tag{10}$$

where, for instance, a_{11} is the component in the first row and column of the $\overline{\overline{A}}$ matrix. If the constants

$$Q = \frac{\sigma}{\epsilon_r\epsilon_0} + (\xi+\eta) \tag{11}$$

$$R = -\zeta \tag{12}$$

$$S = \epsilon_r\epsilon_0\xi\eta + \sigma(\xi+\eta) \tag{13}$$

$$T = \sigma\xi\eta \tag{14}$$

the requisite matrices are

$$\overline{\overline{A}} = \begin{bmatrix} 1.0 & (\Delta t/2\epsilon_r\epsilon_o)\exp(-Q\,\Delta t/2) \\ -S\,\Delta t/2 & 1.0 \end{bmatrix} \quad (15)$$

$$\overline{\overline{B}} = \begin{bmatrix} \exp(-Q\,\Delta t) & -(\Delta t/2\epsilon_r\epsilon_o)(-Q\,\Delta t/2) \\ S\,\Delta t/2 & 1.0 \end{bmatrix} \quad (16)$$

$$\overline{\overline{C}} = \begin{bmatrix} (\Delta t/\epsilon_r\epsilon_o)\exp(-Q\,\Delta t/2) & 0.0 \\ R\,\Delta t & \Delta t \end{bmatrix}. \quad (17)$$

As noted above, similar equations occur for the x- and y-components, which can be obtained immediately from this set by cyclic permutations of the indexes and profile parameters. These equations reduce to the TDLM ABC equations given in [16] when $\sigma \to 0$ and $\epsilon_r \to 1$.

IV. Numerical Results

To benchmark the behavior of the L2TDLM ABC, comparisons with Gedney's UPML ABC were first performed. Similar reflection properties were demonstrated. These results are summarized below. With the aid of the L2TDLM ABC, we then investigated the effect of lossy dielectric substrates in several classes of microstrip structures.

We have chosen a set of previously published [28] microstrip structures for which calculated and measured results have been presented. These structures consist of a microstrip low-pass filter, branch-line coupler, and edge-fed rectangular patch antenna. We proceed by considering each structure in turn. The original results from [28] are reproduced in the absence of conductivity loss. Utilizing the properties of the L2TDLM ABC, we may now introduce the appropriate loss tangent for Duroid 5880; the substrate typically used in the fabrication of these structures. The results of the loss cited by the manufacturer are incorporated in the dielectric substrate used in the simulations. Further, the effects of a loss tangent of 100 times larger than that specified by the manufacturer is examined. This extra step is performed with an eye toward the requirements of full-wave electromagnetic simulators (FDTD and FEM) to accurately model microstrip structures on high loss dielectrics including silicon, alumina, and gallium–arsenide.

For each microstrip structure, the calculation of the scattering parameters was facilitated by first simulating a through line. The microstrip transmission line was modeled in all cases as an infinitely thin conductor in the $z = 4\ \Delta z$ plane, which was $6\ \Delta x$ cells (2.436 mm [0.0959 in]) wide. The conducting strip was extended into the L2TDLM ABC in the $\pm\hat{y}$-directions. The through line was then replaced by the desired structure and the simulation run again. Field values in time were obtained at the same points along the line. The scattering parameters S_{11} and S_{21} were then generated as functions of frequency by Fourier transforming the time history of the field associated with the structure present and the time history of the field associated with the structure absent (reference case) and dividing the resulting spectra. The effect of dielectric loss was investigated by repeating the above process for the two remaining conductivity values. The calculated scattering parameters were then validated by comparison with measurements. Radiation patterns were obtained for the microstrip patch antenna with a near- to far-field transform [29], [30].

The loss tangent $\tan\delta$ of the material was modeled by changing the conductivity of the substrate. The lossless substrate was modeled with a $\sigma = 0$ conductivity value. However, Rogers (the manufacturer of the material) cites a loss tangent of $\tan\delta = 9.0 \times 10^{-4}$ at a frequency of 10 GHz for Duroid 5880. This is equivalent to a $\sigma = 1.1 \times 10^{-3}$ conductivity value. We will refer to this configuration as the "lossy" case. To further investigate the effect of lossy dielectrics, we also simulated the structure with a loss tangent of $\tan\delta = 9.0 \times 10^{-2}$, which is equivalent to a conductivity value of $\sigma = 1.1 \times 10^{-1}$, two orders of magnitude larger than that of the physical material. We will designate this the "very lossy" case.

All of the following planar structures have been modeled on Duroid 5880 with a thickness of 0.795 mm (0.031 in) unless otherwise stated. The dielectric substrate ($\epsilon_r = 2.2$) was modeled three cells thick (0.795 mm [0.0313 in]) in the $\hat{z}$-direction and was extended into the L2TDLM ABC in the xy-plane. Further, the simulation region was truncated using the L2TDLM ABC placed on all faces, except the $-\hat{z}$ face, which was a perfectly electric conductor (PEC) ground plane. The L2TDLM layer was ten cells thick and used a parameter value $\rho_{\max} = 10.0$ (see [1] for details). Note that the number of cells used for the ABC are in addition to the dimensions described below for the simulated microstrip structures.

A. Comparisons with Gedney's UPML ABC

Comparisons between the L2TDLM ABC and the TDLM ABC for the 2-D cases, discussed in [15], and between the UPML ABC for the 2-D cases, discussed in [20] and ([25, Ch. 5]), were run to provide comparison results. A 2-D version of the 3-D L2TDLM ABC is obtained straightforwardly. The update equations are essentially those for the faces and edges, but no auxiliary field variable needs to be introduced into the update system. The out-of-plane component of the electric field is not excited in this reduced dimensionality problem. A code was constructed to test the 2-D L2TDLM ABC. The cases in [15] provided basic algorithmic checks since, as noted above, the L2TDLM ABC reduces to the TDLM ABC when the losses go to zero and the medium becomes free space. All of the results obtained in [15] were reproduced with the L2TDLM ABC algorithm.

Next, Gedney's test case [20], [25, Ch. 5] was considered. It is a two medium problem in which the simulation space is split into two homogeneous half-spaces: one air, the other a lossy medium with $\epsilon_r = 10.0$ and $\sigma = 0.3$ S/m. The normal to the interface is selected to be the $\hat{y}$-direction. The source is a electric dipole strip $J_y(x_c, z_c, t)$ driven with the Gaussian derivative time signal

$$J_y(x_c, z_c, t) = -2\left[\frac{t - t_0}{t_w}\right]\exp\left[-\left(\frac{t - t_0}{t_w}\right)^2\right] \quad (18)$$

where $t_w = 26.53$ ps and $t_0 = 4t_w$. The spectrum of this driving pulse has its peak at an effective frequency of $f_{\text{eff}} = 8.45$ GHz where $\Delta \sim \lambda/35.5$, but extends out to 40 GHz where $\Delta \sim \lambda/7.5$. The strip is oriented along the normal to the interface and is located in the free-space region at two cells above the center of the simulation space. The simulation space consisted of 40×40 square cells and was truncated with a ten-layer quadratic L2TDLM ABC. The reference simulation

region was 1240 × 1240 square cells and was terminated with PECs. The cell size was $\Delta = 0.4$ mm. We introduce a grid frequency $f_{\text{grid}} = c/(40.0\,\Delta_{\max})$, where $\Delta_{\max}$ is the maximum of the cell side lengths Δx, Δy, or Δz; it corresponds to the lowest frequency at which the grid provides a $\lambda/40$ discretization level. Thus, for the cubical grid associated with this problem, $f_{\text{grid}} = 1.875 \times 10^{10}$ Hz. The simulation was run for 1000 time steps, the time step being set at 0.98 of the Courant value. Standard differentiation, while maintaining the semi-implicit formulation, rather than exponential differencing was used to make the 2-D L2TDLM ABC algorithm as close as possible to Gedney's UPML. The problem is treated in a 2-D TE polarization sense; the field components (E_x, E_y, and H_z) are obtained with the FDTD simulator. The maximum relative errors, $\mathcal{E}_A$ and $\mathcal{E}_B$, in E_y are measured, respectively, at the point A, which is located in free space two cells above the interface and two cells from one face of the ABC region, and at the point B, which is located two cells from each face of one of the corners in the lossy medium. The maximum relative error in E_y is defined as the difference in time between the amplitude of E_y for the small problem and for the reference problem normalized by the maximum in time of E_y for the reference result. Note that like Gedney's UPML ABC, only a single maximum parameter is used throughout the L2TDLM ABC. This simplifies the coding requirements significantly. The maximum parameter that gave the best error results in the split-region problem corresponded to the best value for the free-space case.

Using the L2TDLM ABC, it was found that $\mathcal{E}_A = -76.4$ dB and $\mathcal{E}_B = -73.0$ dB with a maximum loss parameter $\rho_{\max}/\omega_{\text{grid}} = 7.13$. Changing the profile of the ABC layers to a quartic variation yielded the errors $\mathcal{E}_A = -85.9$ dB and $\mathcal{E}_B = -71.8$ dB with a maximum loss parameter $\rho_{\max}/\omega_{\text{grid}} = 12.3$. These results are comparable to those reported by Gedney. This problem is a quite difficult one in which to assess the difference in errors between points A and B because the time signals arriving at these two points are dramatically different. The pulse reaching point B is nearly a derivative of the excitation pulse, hence, the peak of its frequency spectrum is upshifted significantly. Moreover, because of the field pattern from the source, different sides of the ABC are illuminated differently. We felt, like Gedney, that these levels of reflection errors are quite satisfactory considering the fact that the discretization is below $\lambda_{\text{medium}}/10$ for a significant portion of the frequency spectrum of the signals reaching the sampling points.

However, to connect these 2-D results with those in [15], [21], and [22], the corresponding line-source problem was also treated. Instead of the electric strip, the problem is now excited by a magnetic line source K_z driven with the time signal used in the cases in [15]:

$$K_z(x_c, z_c, t) = \begin{cases} \dfrac{1}{320}\left[10 - 15\cos(\omega_0 t) + 6\cos(2\omega_0 t) - \cos(3\omega_0 t)\right], \\ \qquad \text{for } 0 \le t \le 1.0 \text{ ns} \\ 0, \qquad \text{for } t > 1.0 \text{ ns} \end{cases} \tag{19}$$

where $\omega_0 = 2.0\pi \times 10^9$. The advantage of this source is that the faces and corners of the simulation region see essentially the same time signal. The cell size was $\Delta = 0.6$ mm; hence, $f_{\text{grid}} = 1.25 \times 10^{10}$ Hz.

In our first series of 2-D simulations, the simulation region was free space. We obtained $\mathcal{E}_A = -96.2$ dB and $\mathcal{E}_B = -74.7$ dB for a maximum loss parameter $\rho_{\max}/\omega_{\text{grid}} = 10.20$ and $\mathcal{E}_A = -84.9$ dB and $\mathcal{E}_B = -81.4$ dB for a maximum loss parameter $\rho_{\max}/\omega_{\text{grid}} = 9.17$. The latter case provided the best overall error performance for a variety of sampling points. These results indicate that the edge and corner errors vary with the choice of the maximum parameter. The more uniform maximum relative error seems to be the most beneficial choice for standard application problems. In our second series of 2-D simulations, the simulation region was completely filled with the lossy dielectric having $\epsilon_r = 10.0$ and $\sigma = 0.3$ S/m. It was found that $\mathcal{E}_A = -92.5$ dB and $\mathcal{E}_B = -91.7$ dB with a maximum loss parameter $\rho_{\max}/\omega_{\text{grid}} = 3.06$, approximately $\sqrt{10}$ smaller than its free-space value. In our third series of 2-D simulations, the simulation region, as it was in Gedney's test case, was half filled with free space and with the same lossy medium. The line source K_z was now excited in free space, two cells away from the center of the simulation region along the normal to the interface. It was found that $\mathcal{E}_A = -93.8$ dB and $\mathcal{E}_B = -81.0$ dB with a maximum loss parameter $\rho_{\max}/\omega_{\text{grid}} = 9.17$. All of these results demonstrate excellent reflectionless behavior.

Finally, we ran our 3-D L2TDLM ABC simulator for the corresponding 3-D problem of a vertical electric dipole located in free space two cells above the same lossy half-space. The simulation space consisted of 40 × 40 × 40 cubic cells and was truncated with a ten-layer quadratic L2TDLM ABC. The reference simulation region was 140 × 140 × 140 cubic cells and was terminated with the same ten-layer quadratic L2TDLM ABC. The cell size was again $\Delta = 0.4$ mm; hence, $f_{\text{grid}} = 1.875 \times 10^{10}$ Hz. The simulation was run for 1000 time steps, the time step being set at the Courant value. The electric dipole was driven with the time signal (18). We obtained $\mathcal{E}_A = -74.7$ dB and $\mathcal{E}_B = -78.6$ dB for a maximum loss parameter $\rho_{\max}/\omega_{\text{grid}} = 9.0$. These results are comparable with those obtained in the 2-D simulations. We note that while the 2-D L2TDLM ABC exhibited much slower growth of the error over the simulation time than Gedney's 2-D UPML ABC, the 3-D L2TDLM ABC simulation showed no growth over the same simulation time.

B. Microstrip Low-Pass Filter

The geometry for the microstrip low-pass filter is given in [28] and repeated here in Fig. 1. The simulation region was 70 × 70 × 16 cells in the $\hat{x}$-, $\hat{y}$-, and $\hat{z}$-directions, respectively. The cell sizes are $\Delta x = 0.406$ mm (0.0160 in), $\Delta y = 0.423$ mm (0.0167 in), and $\Delta z = 0.265$ mm (0.0104 in). This unequal discretization allowed us to model the dimensions of the structure precisely. Since the sampling of the field is so fine for all the frequencies in the excitation pulse ($<\lambda/160$ in the substrate), we expected and found no significant numerical dispersion errors caused by this unequal sampling. The corresponding time step at the $CFL = 1.0$ limit was $\Delta t = 0.655$ psec. The simulation was run for 3000 time steps, resulting in a final time of 1.9655 ns. A current element source with a Gaussian profile was placed

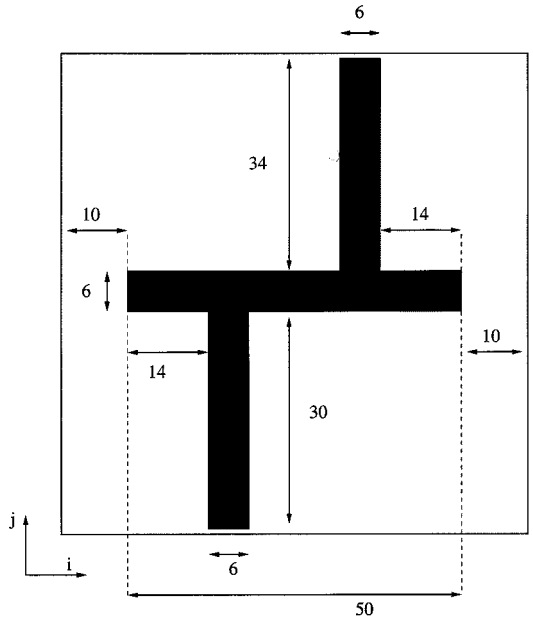

Fig. 1. Dimensions (number of cells) for microstrip low-pass filter.

at the point $(28, 1, 1)$ to locate it exactly in the middle of the microstrip feed line. The $\hat{z}$ component of the electric field was used for the calculation of scattering parameters; it was sampled ten cells (4.23 mm [0.1665 in]) in front of the resonant branch at the point $(28, 20, 2)$ for S_{11} and 26 cells (11.0 mm [0.4330 in]) after the resonant branch at the point $(44, 62, 2)$ for S_{21}. For future reference, we note that this is coincident with the zero phase center of the physical hardware in our test configuration.

The effects of the three values of conductivity on the calculated scattering parameters S_{11} and S_{21} are shown in Fig. 2. The differences between the lossless and lossy cases are indistinguishable. This is to be expected since engineers choose low-loss dielectrics for their designs, and manufacturers go to great lengths to reduce the conductivity loss. Further, this is not a highly resonant structure. The low-pass characteristic is dependent on the electrical length of the center matching section. This length does not change much with the addition of a slight amount of loss. This remark is reinforced through the addition of more loss. In the very lossy case, the resonances and edges of the stopband become rounded and the resonant nulls becoming wider and less defined. This is caused by the "smearing" of the electrical length in the center section of the filter. As expected, the return loss (RL) is increased in the stopband (6–9 GHz) by 1.5–2.0 dB due to the conduction loss. Also, the insertion loss (IL) in the passband (0–5 GHz) is increased by as much as 3 dB at the band edge. We note that for the lossless and lossy cases, the character of the nulls in the IL stopband more closely matched the measured results presented in [28] rather than their calculated results. This further demonstrates the effectiveness of the L2TDLM ABC, even for the lossless case.

Accurate modeling of the dielectric loss in this simple structure only becomes important as the loss becomes large. However, if this structure had been fabricated on silicon or gallium–arsenide, the higher conductivity loss of these materials would have had a greater impact as demonstrated by our very lossy results. A factor of 100 increase in conductivity has resulted in not only reduced overall parameters, but also a consistent frequency down shifting of the resonant nulls. We now identify the importance of being able to correctly model lossy dielectric substrates through the use of appropriate ABCs.

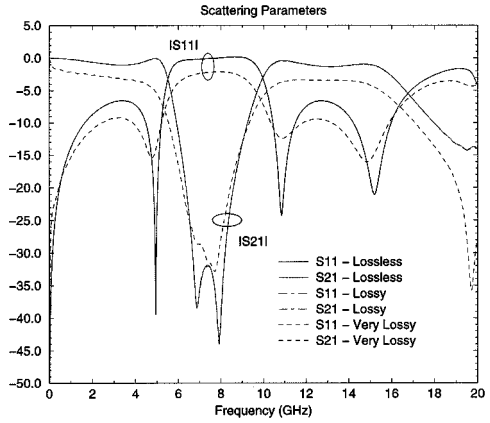

Fig. 2. $|S_{11}|$ and $|S_{21}|$ for microstrip low-pass filter ($\sigma = 0, 1.1 \times 10^{-3}, 1.1 \times 10^{-1}$).

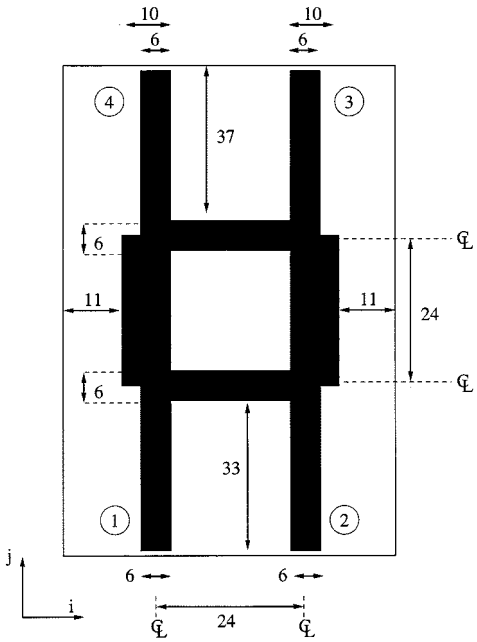

Fig. 3. Dimensions (number of cells) for microstrip branch-line coupler.

C. Microstrip Branch-Line Coupler

The geometry for the branch-line coupler is given in [28] and repeated here in Fig. 3 with the ports labeled. The simulation region was $60 \times 100 \times 16$ cells in the $\hat{x}$-, $\hat{y}$-, and $\hat{z}$-directions, respectively. The cell sizes are $\Delta x = \Delta y = 0.406$ mm (0.0160 in) and $\Delta z = 0.265$ mm (0.0104 in). The corresponding time step at the $CFL = 1.0$ limit was $\Delta t = 0.650$ psec. The simulation was run for 3000 time steps, resulting in a final time of 1.9472 ns. A current element source with a Gaussian profile was placed at the point $(19, 1, 1)$ to locate it exactly in the middle of the feed line. The $\hat{z}$ electric field used for the calculation of scattering parameters was sampled 23 cells (6.1 mm [0.2400 in])

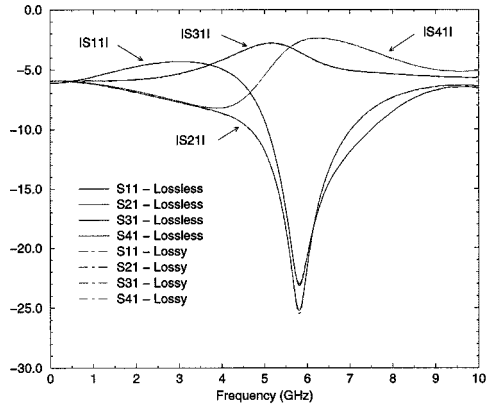

Fig. 4. Scattering parameters for branch-line coupler in the lossless and lossy substrate cases ($\sigma = 0$ and 1.1×10^{-3}).

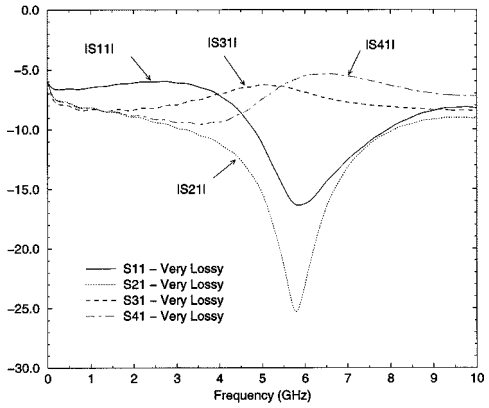

Fig. 5. Scattering parameters for branch-line coupler in the very lossy substrate case ($\sigma = 1.1 \times 10^{-1}$).

away at the point $(19, 24, 2)$. We note that these sampling locations do not coincide with the zero phase centers of the measurements. Justification is presented in the measurements section.

The effects of the three values of conductivity on the calculated scattering parameters S_{11}, S_{21}, S_{31}, and S_{41} are summarized in Fig. 4 for the lossless and lossy cases, and in Fig. 5 for the very lossy case. Again, as shown in Fig. 4, the lossless and lossy cases are almost indistinguishable, except for very small deviations in the nulls of S_{11} and S_{21}.

It is noted that the power from port 1 is divided equally and delivered to ports 3 and 4 only at a single frequency. This frequency is easily located in the figure as the point where S_{31} and S_{41} cross. Ideally, this crossing point occurs at -3 dB, indicating that all of the power from port 1 has been transmitted through the device to ports 3 and 4. The RL at port 1 and the isolation between ports 1 and 2 are symmetric, having equal depth nulls. These properties at a single frequency are characteristic of a balanced structure. Again, these observations are more consistent with the measured data presented in [28] than the calculations provided there. The additional loss realized in the very lossy case shown in Fig. 5 widens and fills the nulls. A slight up shift in the resonance is noted for the very lossy case. The point of equal power delivery to ports 3 and 4 now occurs at a different frequency than where the IL and isolation minimums occur. Again, we find that the accurate modeling of the loss for such a microstrip coupler is only important for the very lossy case where not only are the amplitudes of the scattering parameters effected, but also the frequency at which equal power division, minimum RL, and maximum isolation occurs.

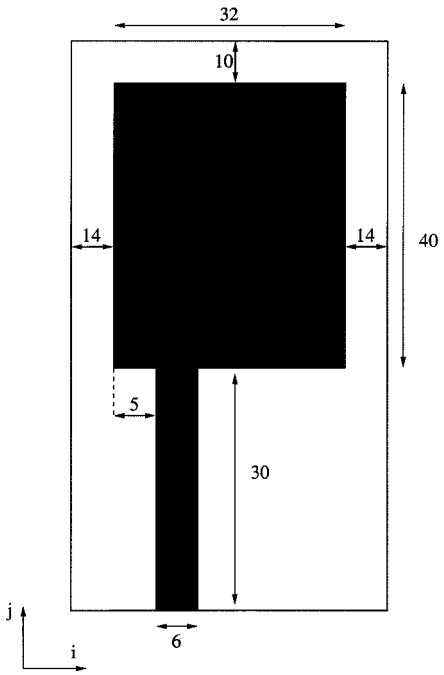

Fig. 6. Dimensions (number of cells) for microstrip edge-fed patch antenna.

D. Microstrip-Line-Fed Rectangular Patch Antenna

The dimensions for the line-fed rectangular patch antenna are given in [28] and repeated here in Fig. 6. The simulation region was $60 \times 90 \times 16$ cells in the $\hat{x}$-, $\hat{y}$-, and $\hat{z}$-directions, respectively. The cell sizes used were $\Delta x = 0.389$ mm (0.0153 in), $\Delta y = 0.400$ mm (0.0158 in), and $\Delta z = 0.265$ mm (0.0104 in). The corresponding time step at the $CFL = 1.0$ limit was $\Delta t = 0.640$ ps. The simulation was run for 3000 time steps, resulting in a final time of 1.9210 ns. A current element source with a Gaussian profile was placed at the point $(23, 1, 1)$ to locate it exactly in the middle of the feed line. The $\hat{z}$ electric field used for the calculation of scattering parameters was sampled 22 cells (8.56 mm [0.3369 in]) away at the point $(23, 25, 2)$.

The results of the scattering parameter calculations for the three conductivity values used in the previous cases are shown in Fig. 7. Although small, the difference between the lossless and lossy case is now discernible at the higher frequencies. However, contrary to the previous two examples involving relatively low-Q structures, the difference in resonant frequencies for the very lossy case is prevalent. While it is true that one would not design such a high-Q structure on a very lossy substrate, this example does demonstrate that resonance is affected by the loss in the dielectric. Thus, it is necessary to have an ABC such as the L2TDLM, which can accurately terminate the simulation region in the presence of lossy dielectrics.

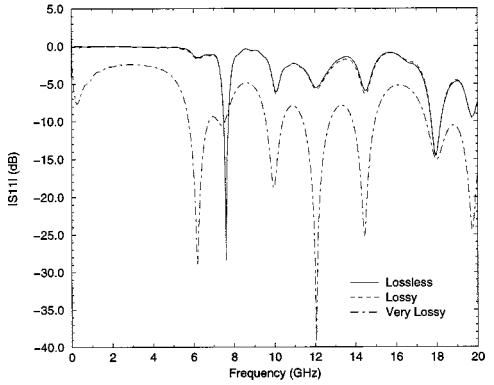

Fig. 7. $|S_{11}|$ for edge-fed rectangular patch antenna ($\sigma = 0$, 1.1×10^{-3}, 1.1×10^{-1}).

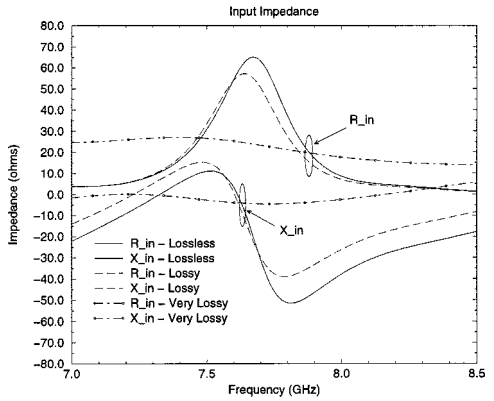

Fig. 8. Input impedance for edge-fed rectangular patch antenna ($\sigma = 0$, 1.1×10^{-3}, 1.1×10^{-1}).

The input impedance of the patch was determined by deembedding the calculated RL S_{11} to the patch edge

$$\frac{Z_{\text{in}}}{Z_o} = \frac{1 + S_{11}\exp(-j2\beta l)}{1 - S_{11}\exp(-j2\beta l)} \tag{20}$$

Z_o is the characteristic impedance of the feeding transmission line and is determined using Wheeler's formula with the above dimensions. The result of this calculation indicates a characteristic impedance of 50 Ω. The propagation constant $\beta = 2\pi f\sqrt{\mu\epsilon_{\text{eff}}}$ is determined on a per frequency basis using an effective $\epsilon_{\text{eff}} = 1.87$, as discussed in [31]. The distance $l = 6.345$ mm is taken from the sampling/measurement plane to the patch edge.

The results of these calculations are shown in Fig. 8 for the lossless, lossy, and very lossy cases. As expected, the high-Q of the patch structure is obviously disturbed by the very lossy case. However, because of our and others experience with scattering parameters, the difference between the lossless and lossy cases was not expected to be so dramatic. Here, it is seen that the inclusion of the small loss effects the amplitude and location in frequency of the simulated input impedance. This is significant and indicates that the inclusion of loss, however small, is important when simulating structures with large Q values. Further, the calculation of some parameters may be more sensitive (such as the impedance calculation) than others (such as the scattering-parameters' calculation). Moreover, it indicates that only dealing with scattering parameters, which are ratio quantities, does not provide a complete picture of the device operation.

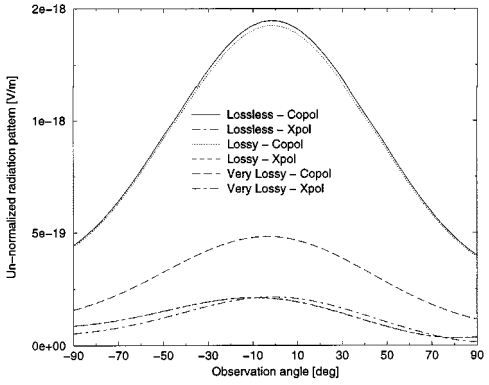

Fig. 9. Radiation patterns for edge-fed rectangular patch antenna ($\sigma = 0$, 1.1×10^{-3}, 1.1×10^{-1}).

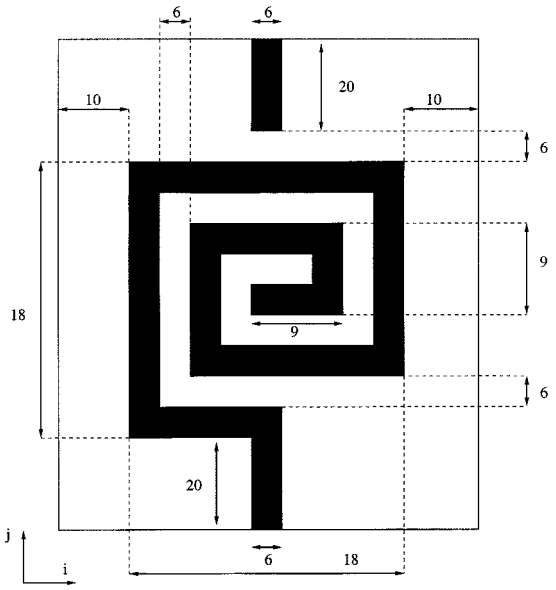

Fig. 10. Dimensions (number of cells) for microstrip rectangular spiral inductor.

The effect of substrate loss on the radiation patterns of the antenna is presented in Fig. 9. The patterns show the E_θ component of the electric field in the co- and cross-polarized planes. These patterns are linear un-normalized plots of the electric-field component. The effect of even a small amount of loss, as in the lossy case, is observed as a diminished intensity in the main beam of the pattern. Substantial loss of intensity in the main beam is experienced for the very lossy case. Finally, the cross-polarization fields are not as drastically effected since they represent only a small portion of the total radiated power.

E. Microstrip Rectangular Spiral Inductor

The dimensions for a rectangular spiral inductor are given in Fig. 10. The simulation region was $70 \times 100 \times 16$ cells in the $\hat{x}$-, $\hat{y}$-, and $\hat{z}$-directions, respectively. The cell sizes are $\Delta x = \Delta y = 0.389$ mm (0.0153 in) and $\Delta z = 0.265$ mm (0.0104 in). The corresponding time step at the $\text{CFL} = 1.0$ limit was

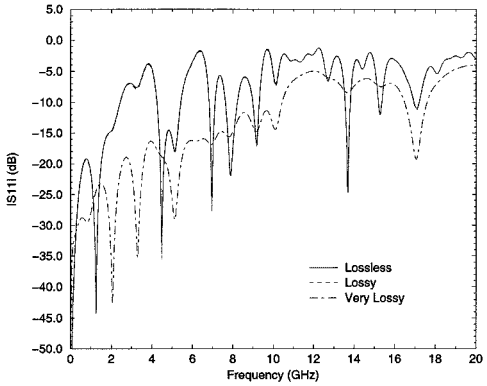

Fig. 11. $|S_{11}|$ for rectangular spiral inductor ($\sigma = 0$, 1.1×10^{-3}, 1.1×10^{-1}).

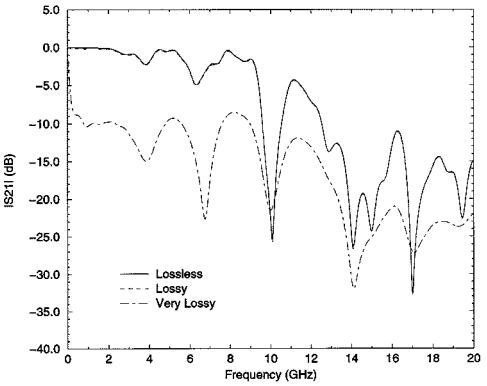

Fig. 12. $|S_{21}|$ for rectangular spiral inductor ($\sigma = 0$, 1.1×10^{-3}, 1.1×10^{-1}).

$\Delta t = 0.636$ ps. The simulation was run for 3000 time steps, resulting in a final time of 1.9085 ns. A current element source with a Gaussian profile was placed at the point $(37, 1, 1)$ to locate it exactly in the middle of the feed line. The $\hat{z}$ electric field used for the calculation of scattering parameters was sampled nine cells (3.50 mm [0.1378 in]) away at the point $(37, 10, 2)$.

The scattering parameters S_{11} and S_{21} were obtained for the three conductivity values used in the previous cases. They are shown in Figs. 11 and 12. Again, the results for the lossless and lossy cases differ only slightly, and there are significant differences between those cases and the very lossy case. These scattering-parameter results were then used to define the inductance, resistance, and Q of the spiral inductor as follows.

The normalized impedance at the input port (defined by the plane used to calculate the scattering parameters) may be computed from the scattering parameter S_{11} by

$$\frac{Z_L}{Z_o} = \frac{1 + S_{11}}{1 - S_{11}} \tag{21}$$

where the normalized port impedance, Z_o is calculated using Wheeler's [31] formula for microstrip transmission lines. This calculation allows us to extract the series resistance R_s and inductance L_s defined by

$$Z_L = R_s + j\omega L_s. \tag{22}$$

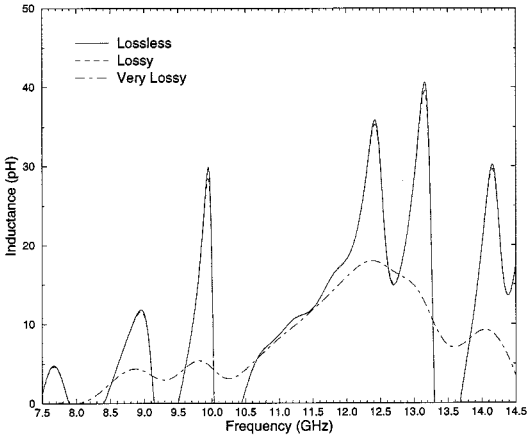

Fig. 13. Series inductance as a function of frequency.

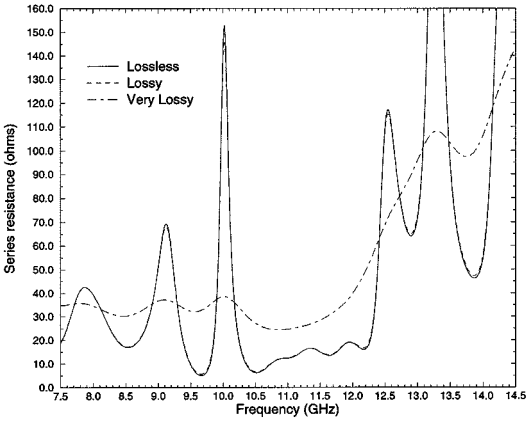

Fig. 14. Series resistance as a function of frequency.

Additionally, the quality factor Q[31] of the structure may be determined by

$$Q = \frac{\omega L_s}{R_s} = \frac{\text{Imag}(Z_L)}{\text{Real}(Z_L)}. \tag{23}$$

The results of the calculations of the inductance, resistance, and Q of the spiral inductor are shown, respectively, in Figs. 13–15. Only inductive values are shown in Fig. 13; values below zero make the structure capacitive. The curves for Q in Fig. 15 indicate that the best operating points for this structure are near 9.5 GHz and between 10.2–11.75 GHz. However, the S_{21} curves in Fig. 12 show that there is a deep null at 9.5 GHz and, hence, that this is not a good operating point for the structure. Fig. 13 shows that the inductance increases almost linearly in the 10.2–11.75-GHz region; Fig. 14 shows that the resistance is nearly constant there. Thus, the simulations indicate that this spiral may be a useful microstrip structure in the frequency range between 10.2–11.75 GHz.

F. Measurement Technique

The above structures were fabricated and measured. The method with which the devices were measured had a significant impact on those results and warrants a detailed explanation; especially in view of the comparisons that will be made. Two

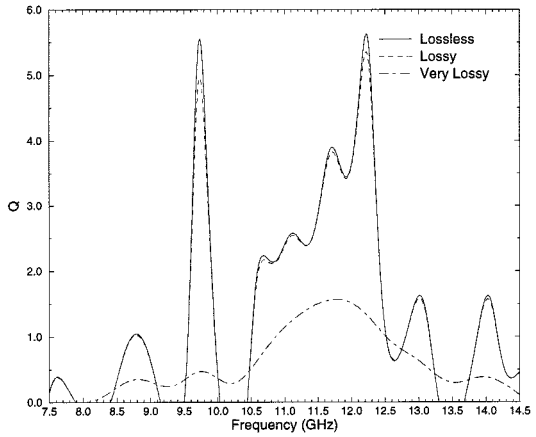

Fig. 15. Quality factor Q as a function of frequency.

different types of measurement calibration methods where used on two different network analyzers to determine the device parameters. The first calibration technique is referred to as short-open-load-thru (SOLT). This is likely the most popular technique used in microwave measurements since it uses a set of standards provided by the manufacturer of the network analyzer. The second calibration technique is referred to as thru-reflect-line (TRL). This type of calibration requires a set of calibration standards to be manufactured by the user and is most typically used when one wishes to remove artifacts from the measurement such as connector and probe discontinuities. Each method has its advantages and will now be discussed in turn.

The popularity of the SOLT calibration stems from the availability of calibration standards provided by the manufacturer of the network analyzer. This relieves the RF engineers from having to design their own calibration standards and, thus, results in fabrication of fewer components and faster measurements. However, the zero phase center of the measurement is placed at the end of the connectors where the calibration was performed. Therefore, discontinuities that occur after this zero phase point and are not intended to be a part of the measurement can produce unwanted artifacts. This is particularly true of microstrip structures that use coaxial connects to attach the circuit to the network analyzer. The discontinuity caused by the coax-to-microstrip transition is then an undesirable addition to the measured device characteristics.

Measurement artifacts introduced by connector and probe discontinuities can be negated by using the TRL calibration method. This method requires the engineer to provide a set of calibration standards, which are fabricated in the same configuration as the device to be tested. For example, measurement of a printed microstrip patch antenna using coaxial connectors requires a set of standards fabricated on the same substrate using the same coax-to-microstrip transition. The standards used in the calibration are composed of a through transmission line, a short or open (usually an open for ease of fabrication), and one or more delay lines. The thru transmission line is chosen to have the same impedance (width) as that which is feeding the device-under-test. The length of this line is arbitrary, but the midpoint of this length will correspond to the zero phase center. Therefore, this length should be selected so that the half-length of the through line is shorter than the feeding line of the device-under-test. The discontinuity, chosen to be an open in this case, is constructed in the same fashion with the open circuit occurring at the same location as the midpoint of the thru line. Finally, delay lines are constructed by choosing a frequency of operation and then selecting a line length that is longer (or shorter) than the through line by a known electrical distance. The electrical length chosen for the delay line(s) must be within the range of $20^\circ \leq \beta l \leq 160^\circ$. For calibrations using a single delay line (as in our case), the first delay line should correspond to $\beta l = 90^\circ$ at the frequency of interest. Additional delay lines may be utilized to improve the calibration bandwidth, but where not examined.

The primary difference between the SOLT and TRL calibrations lies in where the zero phase center is located during the measurement. A simple SOLT calibration places the zero phase center at the ends of the connectors attached to the network analyzer. This has proven to be undesirable because the connector-to-substrate discontinuities effect the measurement. While TRL calibrations require the user to provide their own set of calibration standards, this technique places the zero phase center into the device-under-test and "calibrates out" the connector or probe discontinuities.

Our initial measurements were performed using the SOLT calibration method on both an HP 8510C and a Wiltron 360B network analyzer. The results of these measurements produced much the same result as was published in [28] and simulated here with the exception of some "beating" oscillations about the simulated results. Having verified proper calibration on both analyzers, the beating was determined to be caused by the connector coax-to-microstrip transitions. Thus, the simple SOLT calibration method is not adequate for our purposes. A set of calibration standards was made using a delay line of $\beta l = 90^\circ$ at 5.0 GHz. The TRL calibration was then performed and the devices measured again on the Wiltron analyzer. Using the TRL calibration method removed the beating observed using the SOLT method and produced the measured data presented in the figures.

Finally, it should be noted that the additional use of the Wiltron 3680K universal test fixture (UTF) provided for more repeatable results. The UTF is a holding device used to couple energy into microstrip circuits. The use of this device removes the task of fixturing each circuit with its own connectors and mechanical support. Use of the UTF for each circuit ensures that the connectors and mechanical support remain constant from calibration through test.

G. Measured Versus Simulated Results

Measurement of the devices described above were performed from 2–18 GHz using the TRL calibration technique. The delay line used in the calibration corresponded to $\beta l = 90^\circ$ at 5.0 GHz. Although the measurements spanned 2–18 GHz, the calibration is not accurate all the way to 18 GHz. Verification of the calibration using the through line shows an input match of better then -40 dB up to 11.6 GHz for S_{11}. This calibration also indicates deviations in S_{21} were bounded by 0.05 dB in magnitude up to 11.6 GHz with a 0.15-dB spike in magnitude

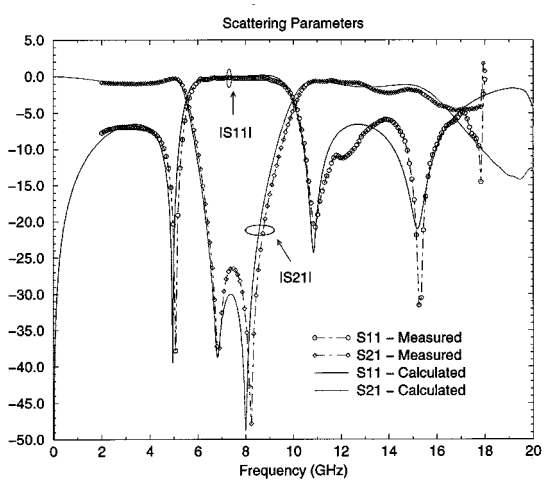

Fig. 16. Measured versus simulated low-pass filter results.

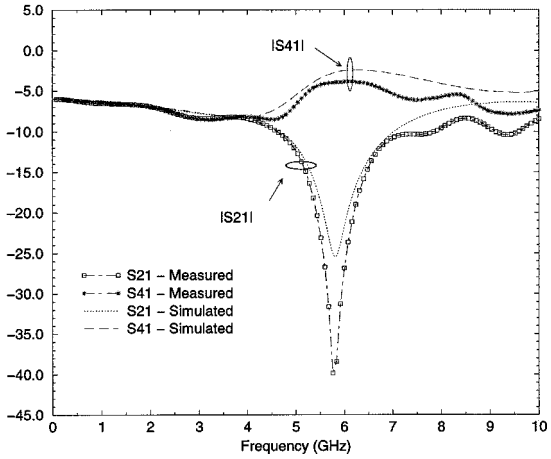

Fig. 18. Measured versus simulated branch-line coupler results B.

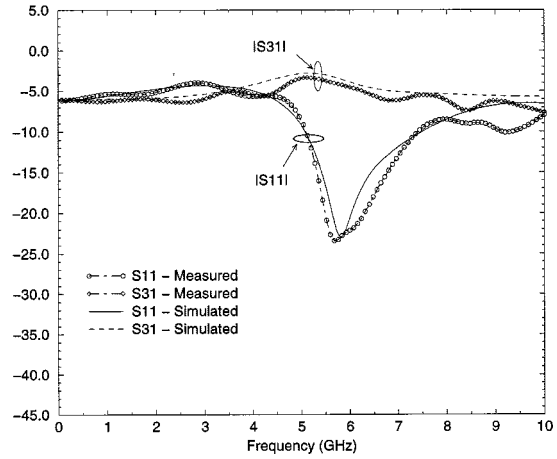

Fig. 17. Measured versus simulated branch-line coupler results A.

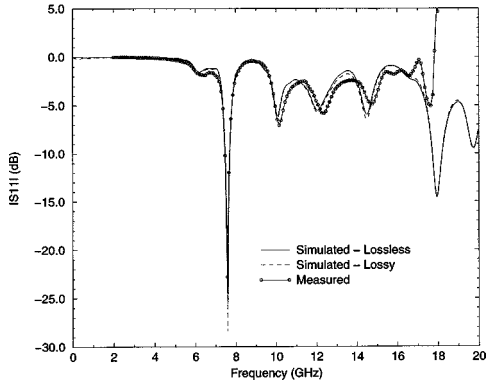

Fig. 19. Measured versus simulated patch antenna results.

at 11.6 GHz. Therefore, differences between measured and simulated results may exist above this frequency. The span of 2–18 GHz was only chosen to correspond with the previously published results.

A comparison of the measured and simulated results for the microstrip low-pass filter is shown in Fig. 16. Observation of the measured versus calculated RL, S_{11}, shows excellent agreement up to 13 GHz with the exception of a slight down shift in frequency of the simulated first resonance of approximately 3.9%. Signal-processing techniques provided no improvements of these conclusions. However, agreement between the simulated and measured results for the IL, S_{21}, is quite good up to the first null. The simulated result predicts the second null to be slightly lower in frequency than the measured result, which further contributes to a variation in the rising edge from 8–10 GHz. Reasonably good agreement is achieved over the remaining portion of the band. Deviations of the measured versus simulated results above 13 GHz are attributed to the inaccuracy of the calibration method over this region.

In the fabrication of the branch-line coupler, it was necessary to extend the transmission line from each port in a radial arc away from its neighboring port. This configuration was necessary to provide mechanical separation of the transmission lines to be fastened to end-launch SMA connectors. Extension of these transmission lines is only believed to effect the isolation between ports 1 and 2 since their proximity to each other was not simulated.

Measurements of the branch-line coupler were obtained using the SOLT calibration technique. The TRL calibration method was not used since our test configuration for this measurement required the UTF, which is only capable of two-port measurements. TRL calibration may be used if the calibration standards and devices-under-test are fabricated with coax-to-microstrip connectors. This option was not explored.

Even with the SOLT calibration, reasonable agreement is obtained between the measured and simulated results, as shown in Figs. 17 and 18. The beating discussed in the measurement section may be observed in these figures as oscillations of the measured data about the simulated data.

A comparison of the measured and simulated results for the microstrip patch antenna is shown in Fig. 19. Excellent agreement is shown in the RL, S_{11}, up to 10 GHz, particularly the first resonance at 7.6 GHz. Above 10 GHz, the simulated results again predict the frequency of the resonances to be slightly lower than the measured results.

Figs. 20 and 21 demonstrate the differences between the measured and simulated results for the spiral inductor. Measured results for the rectangular spiral inductor were obtained using

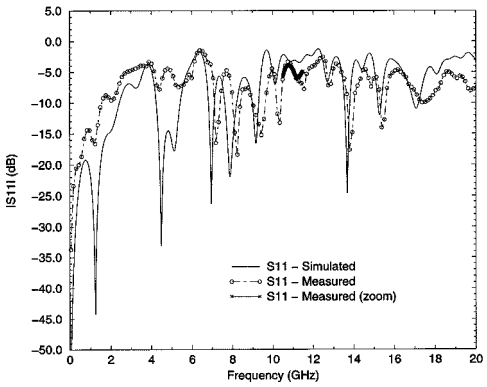

Fig. 20. $|S_{11}|$ for rectangular spiral inductor measured versus simulated.

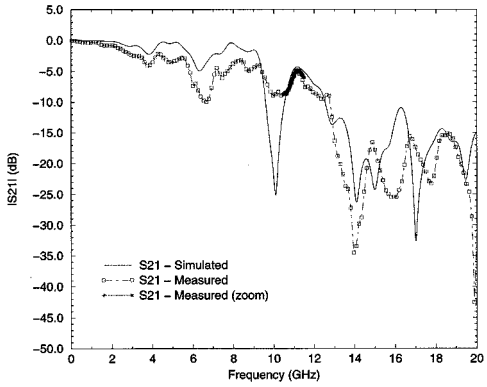

Fig. 21. $|S_{21}|$ for rectangular spiral inductor measured versus simulated.

the SOLT method. A broad-band calibration was performed followed by a more narrow-band calibration about the region of operation identified in the simulation section. Good agreement between measured and simulated results is obtained over the much narrower band, especially for S_{21}. Comparison with simulation shows discrepancies in resonance frequencies and parameter amplitude. The cause for the distant resemblance of the measured and simulated results is believed to result from the air bridge, which is difficult to reliably manufacture. We did not pursue this issue further since we did not have immediate access to the necessary fabrication expertise to produce a reliable air bridge.

V. Conclusions

In this paper, a generalized L2TDLM model ABC was introduced to truncate FDTD simulation regions dealing with lossy dielectric materials. The advantage of the generalized formulation presented here is that only one equation set is required in the implementation for all parts of the ABC region. This equation set reduces to the appropriate formulation (corner to edge to face) dependent on the number of independent parameters present in a given portion of the simulation region. A complete 3-D FDTD implementation was described. It was then applied to a variety of structures, including microstrip lines, filters, couplers, patch antennas, and spiral inductors. Results produced by the L2TDLM ABC augmented FDTD simulator were presented to illustrate when substrate losses become important and how they impact the predicted performance of these microstrip structures. All of the simulated test problems compared well with experimental data. The simulation and experimental results clearly demonstrate that the L2TDLM ABC is a very effective technique for truncating FDTD simulation regions dealing with lossy media. They also demonstrate that lossy ABCs, such as the L2TDLM ABC, are necessary when dealing with resonant structures constructed from high-loss substrates. Neglect of this loss will lead to incorrect performance predictions. We note that conductor losses may play even a bigger role than the substrate losses in the performance of some microwave circuits. They are currently under investigation.

Acknowledgment

The authors wish to thank K. Kaneko-Baker, Raytheon Systems Company, Tucson, AZ, and R. Skaggs, Raytheon Systems Company, Tucson, AZ, for valuable conversations on the fabrication and measurement of the devices presented in this paper.

References

[1] D. C. Wittwer and R. W. Ziolkowski, "Maxwellian material based absorbing boundary conditions for lossy media in 3D," *IEEE Trans. Antennas Propagat.*, vol. 48, pp. 200–213, Feb. 2000.

[2] ——, "Two time-derivative Lorentz material (2TDLM) formulation of a Maxwellian absorbing layer matched to a lossy medium," *IEEE Trans. Antennas Propagat.*, vol. 48, pp. 192–199, Feb. 2000.

[3] J.-P. Berenger, "A perfectly matched layer for the absorption of electromagnetic waves," *J. Comput. Phys.*, vol. 114, pp. 185–200, Oct. 1994.

[4] D. S. Katz, E. T. Thiele, and A. Taflove, "Validation and extension to three dimensions of the Berenger PML absorbing boundary condition for FD-TD meshes," *IEEE Microwave Guided Wave Lett.*, vol. 4, pp. 268–270, Aug. 1994.

[5] W. C. Chew and W. H. Weedon, "A 3D perfectly matched medium from modified Maxwell's equations with stretched coordinates," *Microwave Opt. Technol. Lett.*, vol. 7, no. 9, pp. 599–604, Sept. 1994.

[6] C. E. Reuter, R. M. Joseph, E. T. Thiele, D. S. Katz, and A. Taflove, "Ultrawideband absorbing boundary condition for termination of waveguiding structures in FD-TD simulations," *IEEE Microwave Guided Wave Lett.*, vol. 4, pp. 344–246, Oct. 1994.

[7] C. M. Rappaport, "Perfectly matched absorbing boundary conditions based on anisotropic lossy mapping of space," *IEEE Microwave Guided Wave Lett.*, vol. 5, pp. 90–92, Mar. 1995.

[8] R. Mittra and Ü. Pekel, "A new look at the perfectly matched layer (PML) concept for the reflectionless absorption of electromagnetic waves," *IEEE Microwave Guided Wave Lett.*, vol. 5, pp. 84–86, Mar. 1995.

[9] Z. S. Sacks, D. M. Kingsland, R. Lee, and J.-F. Lee, "A perfectly matched anisotropic absorber for use as an absorbing boundary condition," *IEEE Trans. Antennas Propagat*, vol. 43, pp. 1460–1463, Dec. 1995.

[10] D. C. Wittwer and R. W. Ziolkowski, "How to design the imperfect Berenger PML," *Electromag.*, vol. 16, pp. 465–485, July–Aug. 1996.

[11] S. Gedney, "An anisotropic perfectly matched layer-absorbing medium for the truncation of FDTD lattices," *IEEE Trans. Antennas Propagat.*, vol. 44, pp. 1630–1639, Dec. 1996.

[12] L. Zhao and A. C. Cangellaris, "GT-PML: Generalized theory of perfectly matched layers and its application to the reflectionless truncation of finite-difference time-domain grids," *IEEE Trans. Microwave Theory Tech.*, vol. 44, pp. 2555–2563, Dec. 1996.

[13] R. W. Ziolkowski, "The design of Maxwellian absorbers for numerical boundary conditions and for practical applications using engineered artificial materials," *IEEE Trans. Antennas Propagat.*, vol. 45, pp. 656–671, Apr. 1997.

[14] ——, "Time-derivative Lorentz materials and their utilization as electromagnetic absorbers," *Phys. Rev. E, Stat. Phys. Plasmas Fluids Relat. Interdiscip. Top.*, vol. 55, no. 6, pp. 7696–7703, June 1997.

[15] ——, "Time-derivative Lorentz material model-based absorbing boundary condition," *IEEE Trans. Antennas Propagat.*, vol. 45, pp. 1530–1535, Oct. 1997.

[16] ——, "Maxwellian material based absorbing boundary conditions," *Comput. Methods Appl. Mech. Eng.*, vol. 169, no. 3–4, pp. 237–262, Feb. 1999.
[17] E. Turkel and A. Yefet, "Absorbing PML boundary layers for wave-like equations," *Appl. Numer. Math.*, vol. 27, no. 4, pp. 533–557, Aug. 1998.
[18] S. Abarbanel and D. Gottlieb, "On the construction and analysis of absorbing layers in CEM," in *Proc. Appl. Comput. Electromag. Soc.*, Monterey, CA, Mar. 1997, pp. 876–883.
[19] P. G. Petropoulos, A. C. Cangellaris, and L. Zhao, "A reflectionless sponge layer absorbing boundary condition for the solution of Maxwell's equations with high-order staggered finite difference schemes," *J. Comput. Phys.*, vol. 139, no. 1, pp. 184–208, Jan. 1998.
[20] S. D. Gedney, "An anisotropic PML absorbing media for FDTD simulation of fields in lossy dispersive media," *Electromag.*, vol. 16, pp. 399–415, July–Aug. 1996.
[21] Y. C. Lau, M. S. Leong, and P. S. Kooi, "Extension of Berenger's PML boundary condition in matching lossy medium and evanescent waves," *Electron. Lett.*, vol. 32, no. 11, pp. 974–976, 1996.
[22] J. Fang and Z. Wu, "Generalized perfect matched layer for the absorption of propagating and evanescent waves in lossless and lossy media," *IEEE Trans. Microwave Theory Tech.*, vol. 14, pp. 2216–2222, Dec. 1996.
[23] Q. H. Liu, "An FDTD algorithm with perfectly matched layers for conductive media," *Microwave Opt. Technol. Lett.*, vol. 14, pp. 134–137, Feb. 1997.
[24] C. M. Rappaport and S. C. Winton, "Modeling dispersive soil for FDTD computation by fitting conductivity parameters," in *Proc. Appl. Comput. Electromag. Soc.*, Monterey, CA, Mar. 1997, pp. 112–117.
[25] A. Taflove, *Advances in Computational Electrodynamics: The Finite-Difference Time-Domain Method*. Norwood, MA: Artech House, 1998.
[26] F. Auzanneau and R. W. Ziolkowski, "Theoretical study of synthetic bianisotropic materials," *J. Electromag. Waves Applicat.*, vol. 12, no. 3, pp. 353–370, Dec. 1997.
[27] ——, "Microwave signal rectification using artificial composite materials composed of diode-loaded, electrically small dipole antennas," *IEEE. Trans. Microwave Theory Tech.*, vol. 46, pp. 1628–1637, Nov. 1998.
[28] D. M. Sheen, S. M. Ali, M. D. Abouzahra, and J. A. Kong, "Application of the three-dimensional finite-difference time-domain method to the analysis of planar microstrip circuits," *IEEE Trans. Microwave Theory Tech.*, vol. 38, pp. 849–857, July 1990.
[29] M. J. Barth, R. R. McLeod, and R. W. Ziolkowski, "A near and far-field projection algorithm for finite-difference time-domain codes," *J. Electromag. Waves Applicat.*, vol. 6, pp. 5–18, Jan. 1992.
[30] A. Taflove, *Computational Electrodynamics*. Norwood, MA: Artech House, 1995.
[31] D. M. Pozar, *Microwave Engineering*. Reading, MA: Addison-Wesley, 1990.

David C. Wittwer (M'93) received the B.S., M.S., and Ph.D. degrees in electrical engineering from the University of Arizona, Tucson, in 1993, 1995, and 1998, respectively

From 1995 to 1999, he was a Member of the Technical Staff at the Hughes Missile Systems Company, Tucson, AZ, where he was involved with the analysis, design, and measurement of microstrip and slot arrays for missile seeker and telemetry antennas. In 1999, he joined the Assembly and Test Development Group, Intel Corporation, Chandler, AZ, where he is currently a Senior Packaging Engineer. His focus area is in electromagnetic compatibility and interference compliance of computer microprocessors. His research interests include the development and implementation of time-domain electromagnetic solvers.

Dr. Wittwer is a member of the IEEE Antennas and Propagation Society (IEEE AP-S), the IEEE Microwave Theory and Techniques Society (IEEE MTT-S), and the IEEE Electromagnetic Compatibility Society. He was the recipient of a Howard Hughes Doctoral Fellowship.

Richard W. Ziolkowski (M'87–SM'91–F'94) received the Sc.B. degree in physics (*magna cum laude* with honors) from Brown University, Providence, RI, in 1974, and the M.S. and Ph.D. degrees in physics from the University of Illinois at Urbana-Champaign in 1975 and 1980, respectively.

From 1981 to 1990, he was a Member of the Engineering Research Division, Lawrence Livermore National Laboratory, and served as the Leader of the Computational Electronics and Electromagnetics Thrust Area for the Engineering Directorate from 1984 to 1990. He joined the Department of Electrical and Computer Engineering, University of Arizona, Tucson, as an Associate Professor in 1990, and was promoted to Full Professor in 1996. His research interests include the application of new mathematical and numerical methods to linear and nonlinear problems dealing with the interaction of acoustic and electromagnetic waves with realistic materials and structures. He was a co-guest editor of the 1998 feature issue on "Mathematics and Modeling in Modern Optics" of the *Journal of the Optical Society of America A*.

Prof. Ziolkowski is a member of the Tau Beta Pi, Sigma Xi, Phi Kappa Phi, the American Physical Society, the Optical Society of America, the Acoustical Society of America, and Commissions B (Fields and Waves) and D (Electronics and Photonics) of the International Union of Radio Science (URSI). He was an associate editor for the IEEE TRANSACTIONS ON ANTENNAS AND PROPOGATION (1993–1998). He served as the vice chairman of the 1989 IEEE/AP-S and URSI Symposium, San Jose, CA, and as the technical program chairperson for the 1998 IEEE Conference on Electromagnetic Field Computation, Tucson, AZ. He is currently a member of the IEEE AP-S Administrative Committee (AdCom). For the US URSI Commission B, he served as secretary (1993–1996) and as chairperson of the Technical Activities Committee (1997–1999). He is currently a member-at-large of the U.S. National Committee (USNC) of the URSI. He was co-organizer of the Photonics Nanostructures Special Symposia at the 1998, 1999, and 2000 Optical Society of America (OSA) Integrated Photonics Research Topical Meetings. He was the recipient of the 1993 Tau Beta Pi Professor of the Year Award and the 1993 and 1998 IEEE and Eta Kappa Nu Outstanding Teaching Award.